BOX SPLINE WAVELET FRAMES FOR IMAGE EDGE ANALYSIS

WEIHONG GUO* AND MING-JUN LAI†

Abstract. We present a new box spline wavelet frame and apply it for image edge analysis. The wavelet frame is constructed using a box spline of eight directions. It is tight and has seldom been used for applications. Due to the eight different directions, it can find edges of various types in detail quite well. In addition to step edges (local discontinuities in intensity), it is able to locate Dirac edges (momentary changes of intensity) and hidden edges (local discontinuity in intensity derivatives). The method is simple and robust to noise. Many numerical examples are presented to demonstrate the effectiveness of this method. Quantitative and qualitative comparison with other edge detection techniques are provided to show the advantages of this wavelet frame. Our test images include synthetic ones with known ground truth and natural, medical images with rich geometric information.

Key words. Edge detection, box spline, wavelet frames, step edge, Dirac edge

1. Introduction. Edge detection is consistent with human perception and is usually the first step for image interpretation and understanding. Edges provide the topology and structure information of essential objects in an image. In other words, edges present the skeleton of an image. Edge information can be used directly for feature extraction, object identification, region segmentation, etc. It can also be used as a priori information to help improve other tasks such as image denoising, image restoration, image reconstruction, pattern recognition, etc. The general edge detection task recovers step edges (local discontinuities in intensity), Dirac edges (momentary changes of intensity), as well as other edges such as hidden edges (discontinuous locations of some directional derivatives of images). Certainly, edge detectors produce edges with some compromise among accuracy, completeness, and smoothness, etc. The goal of this research is to find the details of an image as accurately as possible.

In this paper, we present an edge detector based on box spline wavelet frames. We show that it is able to detect edges very well. An advantage of using frames is that they consist of many redundant functions which can approximate various edges and features better than using linearly independent functions. Box splines are compactly supported piecewise polynomial functions. They are smooth and refinable and hence are often used to construct various wavelet functions such as bi-orthogonal wavelets, pre-wavelets, tight wavelet frames in multivariate setting (cf. see [20, 25, 29] for their explicit formulas with any degrees of regularity). Although it has been known for several years that wavelet functions can be used for image edge detection, the performance and effectiveness of box spline wavelet frames for such applications are not well understood. In particular, it is not known which box spline wavelet frame works the best for edge extraction. Following the construction method in [29] and the work [35], we have obtained box spline wavelet framelets based on various box splines $B_{111}, B_{221}, B_{222}, B_{1111}, B_{2111}, B_{2211}$ on a three and a four direction mesh (cf. [14] or [28]) and B_8, which is a box spline based on eight different directions to be explained in section 3.

We have tested these wavelet frames as well as those based on the tensor product of univariate linear, quadratic, cubic and quadratic B-splines for edge detection on various images. The experiments show that B_8 is most effective in catching the details of images. Qualitative and quantitative comparisons with some other types of edge detectors, such as Canny, Prewit, and shearlet based methods, show that the proposed box spline edge detector produces more accurate edges under similar conditions. For the sake of fair comparison, we start with a synthetic image with ground truth edges, and apply four edge detectors under various parameter settings to this image. We then compare the best results of the four methods using *Pratt's figure of merit* (Figure 4.1) and compare results under various parameter settings using *probability of detection* (Figure 4.2). These comparison results show that the proposed edge detector leads to higher figure of merit and consistently higher probability of detection. Visual qualitative comparisons on other natural images (Figures 4.3 - 4.9) imply that the proposed edge detector is able to catch fine details and is robust to noise. We explain the details in section 3 and demonstrate the results in section 4 with various applications.

The paper is organized as follows: we start with a literature review of some edge detection methods in section 2. Section 3 discusses the construction of box spline wavelet frames, and how to use them to remove noise and to detect edges. In particular, we introduce a new box spline function based on a eight direction

*Department of Mathematics, Case Western Reserve University, Cleveland, OH, 44106, USA. (wxg49@case.edu).
†Department of Mathematics, The University of Georgia, Athens, GA 30602, USA. (mjlai@math.uga.edu)

mesh and use it to construct wavelet frames. In section 4, we compare the proposed box spline edge detector with several others, and demonstrate that the proposed approach always performs best in capturing the details of images. In addition we present examples to find hidden edges of images in section 4.4. Finally, conclusions are drawn in section 5.

2. Review on edge detectors. In this section we review some existing edge detectors.

2.1. Partial derivative based edge detectors. An important class of existing edge detectors is based on partial derivatives of the input image. Image pixels with maximum gradients or zero Laplacians are classified as edges [3, 15, 21, 30, 33, 22]. These gradient based edge detectors typically include three steps. First, reduce noise if the input image is noisy; usually a Gaussian convolution is applied. Second, the partial derivatives are estimated by convolving with some kernels. Various kernels have been developed for this purpose with different accuracies along different directions (cf. [50, 48]). Prewit and Canny edge detectors for instance differ only in the kernels used to approximate the partial derivatives. Third, edges are located where the norms of the gradients are above a threshold. Standard thresholding techniques treat pixels with gradient magnitude greater than a threshold as edges. Hysteresis thresholding uses two different thresholds. Any pixel with gradient magnitude above the larger threshold is characterized as edge, so are those pixels that are in the neighborhood of this pixel and with their gradient magnitudes higher than the smaller threshold. This hysteresis thresholding technique leads to connected edges and is sometimes referred to as linking. Non-maximum suppression is sometimes used to thin edges in a method such as the Canny method.

Edge detectors of this type are robust to low-level noise, but they tend to mistakenly detect fake edges due to excessive noise/artifacts. To alleviate this issue, one can further incorporate local mutual information (cf. e.g. [18]).

2.2. Continuous wavelet based edge detector and shearlet based edge detector. Mallat's wavelet based method [32] can detect both the location and the types (such as step and Dirac) of edges through analyzing *local Lipschitz regularity*, a quantity related to how fast the wavelet transfrom coefficients change across scales. We first briefly review the definition of Lipschitz regularity and wavelet transform, followed by reviewing a theorem that relates the two of them. Refer to [32] for more details.

DEFINITION 2.1 (Lipschitz regularity). *Let $0 \le \alpha \le 1$. A function $f(x)$ is uniformly Lipschitz α over an interval (a, b) if there exists a constant C such that for any $x_0, x_1 \in (a, b)$, $|f(x_0) - f(x_1)| \le C|x_0 - x_1|^\alpha$. The Lipschitz regularity of $f(x)$ is defined as the upper bound α_0 of all α satisfying the above condition.*

The Lipschitz regularity of a function is related to continuity/singularity. For instance, if $f(x)$ is differentiable at x_0, then it is Lipschitz 1 near x_0. Lipschitz regularity is difficult to verify directly but Mallat et al. propsed a theorem to relate the local Lipschitz regularity with the dyadic wavelet transform. Recall that a nonzero function $\omega \in L^1(\mathbb{R})$, is called a wavelet if $\int_{-\infty}^{\infty} \omega(x)dx = 0$ (cf. [12], p. 3). With a wavelet function, we can define the wavelet transform as follows:

DEFINITION 2.2 (Wavelet transform). *Let ω be a wavelet function. The continuous wavelet transform of f with respect to ω at scale s is defined as $W_s f(x) := \int_{-\infty}^{\infty} f(y)\frac{\omega((y-x)/s)}{s}dy$. For dyadic wavelet transforms, the scale s is chosen as $s = 2^j$ and $x = 2^j n$ for $j, n \in \mathbb{Z}$.*

A wavelet transform can be used to characterize local regularities of functions. See Theorem 1 in [32] and/or Theorems 2.91–2.92 in [12] for a proof of the following theorem:

THEOREM 2.3. *Let $0 < \alpha \le 1$. A function $f(x)$ is uniformly Lipschitz α over (a, b) if and only if there exists a constant $K > 0$ such that the wavelet transform satisfies $|W_{2^j} f(x)| \le K(2^j)^\alpha$, for all $x \in (a, b)$, and $j = 1, 2, \cdots$.*

According to this theorem, if a function f has a Lipschitz regularity for $0 < \alpha \le 1$, the value of $\sup_{x\in(a,b)} |W_{2^j} f(x)|$ should decrease as the scale j decreases. If $\sup_{x\in(a,b)} |W_{2^j} f(x)|$ increases instead, then f does not have a Lipschitz regularity and thus must have an impulse (Dirac) at x. If $\sup_{x\in(a,b)} |W_{2^j} f(x)|$ does not change much across the scales, it indicates that $\alpha = 0$ and there is a jump at x. These facts form a basis for using a wavelet transform to detect edges.

On the other hand, it is known that a continuous wavelet based edge detector has difficulty in distinguishing nearby edges and has a poor angular accuracy (cf. [32]). It is due to the well-known fact that

wavelets are perfect in describing *isotropic* structures, but not so well in dealing with *anisotropic* phenomena. More recently, shearlets [16, 23] have been used for edge detection and analysis (cf. [47]). It claims to be effective in detecting the location, orientation of edges as well as the number of edges at each point. A shearlet transform decomposes an image with respect to scale, location and orientation. The orientation information at each scale is directly available. The locations of image edges are then determined by the changes in shearlet transform coefficients across scales. The orientations of edges are extracted from the directions in which the shearlet transform coefficients are significant, while the number of edges at each point is determined by the number of peaks of the shearlet transform coefficients.

2.3. Segmentation based edge detectors. Although image segmentation is different from edge detection, they are related and one can also extract edges from the segmentation results. Image segmentation [34, 2, 4] partitions the image domain into different subregions, that are each homogeneous with respect to some characteristics such as intensity. The borders of those subregions form the edges. To give more mathematical details, we take the 2-phase Mumford-Shah method as an example. Let g be the intensity function of an input image. The method separates the image domain into two parts Ω_1 and Ω_2, one inside the edge contour Γ and the other one outside, such that g can be approximated by C^1 functions f_1, f_2 in Ω_1, Ω_2 respectively. The separation is done by minimizing the following functional

$$E(f_1, f_2, \Gamma) = \frac{1}{2}\int_{\Omega_1}(g-f_1)^2 + \frac{1}{2}\int_{\Omega_2}(g-f_2)^2 + \alpha\int_{\Omega_1}|\nabla f_1|^2 + \alpha\int_{\Omega_2}|\nabla f_2|^2 + \beta\cdot\text{Length}(\Gamma)$$

with respect to functions f_1, f_2 and contour Γ. In the special case where f_1, f_2 are constant with values c_1, c_2 respectively, the implementation of the Mumford-Shah model is simplified by the Chan-Vese method [4] based on the level set approach (cf. [36]). It represents the edge contour Γ by the zero level set of a Lipschitz function $\Phi : \Omega \to \mathbb{R}$ and the regions inside and outside of the contour Γ by the regions with positive and negative Φ values respectively. Let $H(\cdot)$ be the Heaviside function defined as $H(z) = 1$ for positive z and 0 elsewhere. Then the minimizer Φ of

$$\frac{1}{2}\int_{\Omega}[H(\Phi)(g-c_1)^2 + (1-H(\Phi))(g-c_2)^2] + \beta\int_{\Omega}|\nabla H(\Phi)|$$

gives the segmentation of the domain and the edge contours. The edges are detected from the 0 level set of Φ.

2.4. Other methods. Other edge detection approaches include Mumford-Shah green function [31], morphological gradient [42, 37, 39], fractal geometry [49, 45], and high-order and variable-order total variation [43] based methods.

3. Box spline tight wavelet frames. Tight wavelet frames are the generalizations of discrete orthonormal wavelets [40, 41, 9, 10, 11, 13, 35, 29, 27]. An advantage of using frames is that they consist of many redundant functions which can approximate various edges and features better than using only linearly independent functions. Box splines are refinable functions, and one can easily choose various directions to obtain a box spline function with a desired order of smoothness ([14], Chapter 12 of [28], [24]). They have been used to construct various wavelet functions including tight wavelet frames. In this section, we first review general box spline tight wavelet frames and then present our derivation of a new box spline wavelet frame based on B_8.

3.1. Review on general box spline tight wavelet frames. We begin with the definition of tight wavelet frames based on multi-resolution approximation of $L_2(\mathbb{R}^2)$. Given a function $\psi \in L_2(\mathbb{R}^2)$, we define

$$\psi_{j,k}(y) = 2^j\psi(2^j y - k)$$

with $k \in \mathbb{Z}^2$ a translation, and $j \in \mathbb{Z}$ a dilation. Let Ψ be a finite subset of $L_2(\mathbb{R}^2)$ and $\Lambda(\Psi) := \{\psi_{j,k}, \psi \in \Psi, j \in Z, k \in Z^2\}$.

DEFINITION 3.1. *We say that $\Lambda(\Psi)$ is a frame if there exist two positive numbers A and B such that*

$$A\|f\|^2_{L_2(\mathbb{R}^2)} \le \sum_{g\in\Lambda(\Psi)}|\langle f, g\rangle|^2 \le B\|f\|^2_{L_2(\mathbb{R}^2)}$$

for all $f \in L_2(\mathbb{R}^2)$. $\Lambda(\Psi)$ is a tight frame if it is a frame with $A = B$. In this case, after a renormalization of the g's in Ψ, we have

$$\sum_{g\in\Lambda(\Psi)} |\langle f, g\rangle|^2 = \|f\|^2_{L_2(\mathbb{R}^2)}$$

for all $f \in L_2(\mathbb{R}^2)$.

It is known by the polarization identity (cf. [12], p. 101) that when $\Lambda(\Psi)$ is a tight frame, any $f \in L_2(\mathbb{R}^2)$ can be represented by $g \in \Lambda(\Psi)$ in the following format:

$$f = \sum_{g\in\Lambda(\Psi)} \langle f, g\rangle g, \quad \forall f \in L_2(\mathbb{R}^2).$$

Let $\phi \in L_2(\mathbb{R}^2)$ be a compactly supported refinable function, i.e. ϕ satisfies the following refinable equation:

$$\hat{\phi}(\omega) = P(\omega/2)\hat{\phi}(\omega/2),$$

where $\hat{\phi}$ is the Fourier transform of ϕ and $P(\omega)$ is a Laurent polynomial in $e^{i\omega} = (e^{i\xi}, e^{i\eta})$. P is often called the mask of a refinable function ϕ. We look for another Laurent polynomial Q_i such that

$$P(\omega)\overline{P(\omega+\ell)} + \sum_{i=0}^{r} Q_i(\omega)\overline{Q_i(\omega+\ell)} = \begin{cases} 1, & \text{if } \ell = 0, \\ 0, & \ell \in \{0,1\}^2\pi\backslash\{0\}. \end{cases} \tag{3.1}$$

The conditions (3.1) are called the *Unitary Extension Principle (UEP)* as in [40], [41] and [13]. With these Q_i's we can define wavelet frame generators or framelets $\psi^{(i)}$ in terms of the Fourier transform by

$$\hat{\psi}^{(i)}(\omega) = Q_i(\omega/2)\hat{\phi}(\omega/2), \quad i = 1, \ldots, r. \tag{3.2}$$

Then, if ϕ has Lipschitz regularity with $\alpha > 0$, $\Psi = \{\psi^{(i)}, i = 1, \ldots, r\}$ generates a tight frame, i.e., $\Lambda(\Psi)$ is a tight wavelet frame (cf. [29]).

Furthermore, assuming $\omega = (\xi, \eta)$ and letting $\mathcal{Q}$ be a rectangular matrix defined by

$$\mathcal{Q} = \begin{bmatrix} Q_1(\xi,\eta) & Q_1(\xi+\pi,\eta) & Q_1(\xi,\eta+\pi) & Q_1(\xi+\pi,\eta+\pi) \\ Q_2(\xi,\eta) & Q_2(\xi+\pi,\eta) & Q_2(\xi,\eta+\pi) & Q_2(\xi+\pi,\eta+\pi) \\ Q_3(\xi,\eta) & Q_3(\xi+\pi,\eta) & Q_3(\xi+\pi,\eta) & Q_3(\xi+\pi,\eta+\pi) \\ Q_4(\xi,\eta) & Q_4(\xi+\pi,\eta) & Q_4(\xi+\pi,\eta) & Q_4(\xi+\pi,\eta+\pi) \\ \vdots & \vdots & \vdots & \vdots \\ Q_r(\xi,\eta) & Q_r(\xi+\pi,\eta) & Q_r(\xi+\pi,\eta) & Q_r(\xi+\pi,\eta+\pi) \end{bmatrix}, \tag{3.3}$$

and $\mathcal{P} = (P(\xi,\eta), P(\xi+\pi,\eta), P(\xi,\eta+\pi), P(\xi+\pi,\eta+\pi))^\top$, (3.1) is simply

$$\overline{\mathcal{P}}\mathcal{P}^\top + \mathcal{Q}^*\mathcal{Q} = I_{4\times 4}, \tag{3.4}$$

i.e.,

$$\sum_{\ell\in\{0,1\}^2\pi} |P(\omega+\ell)|^2 = 1. \tag{3.5}$$

The construction of tight wavelet frames involves finding the $\mathcal{Q}$ that satisfies (3.4), which is called a perfect reconstruction condition. It was observed in [29] that $\mathcal{Q}$ can be easily found if $\mathcal{P}$ satisfies the QMF condition $\mathcal{P}^T\mathcal{P} = 1$, i.e., $\sum_{\ell\in\{0,1\}^2\pi} |P(\omega+\ell)|^2 = 1$. In this case, $\mathcal{Q}$ has a very simple expression. However, the mask P of a refinable function ϕ usually does not satisfy the QMF condition but the following *sub-QMF condition* instead:

$$\sum_{\ell\in\{0,1\}^2\pi} |P(\omega+\ell)|^2 \le 1. \tag{3.6}$$

For example, the masks of bivariate box splines on a three, a four and a eight direction mesh below satisfy (3.6). Recall that any Laurent polynomial $P(\omega)$ can be rewritten as the following:

$$P(\omega) = P_{(0,0)}(2\omega) + e^{i\xi}P_{(1,0)}(2\omega) + e^{i\eta}P_{(0,1)}(2\omega) + e^{i(\xi+\eta)}P_{(1,1)}(2\omega)$$

for some $P_m, m \in \{0,1\}^2$. These $P_m(\cdot)$ are called polyphases of $P(\cdot)$.

THEOREM 3.2 (Lai and Stöckler, 2006). *Suppose that P satisfies the sub-QMF condition (3.6) and that there exists Laurent polynomials $\tilde{P}_1, \ldots, \tilde{P}_N$ such that*

$$\sum_{m\in\{0,1\}^2} |P_m(\omega)|^2 + \sum_{i=1}^{N} |\tilde{P}_i(2\omega)|^2 = 1, \tag{3.7}$$

where $P_m, m \in \{0,1\}^2$ are polyphases of P. Then there exist $4+N$ compactly supported tight frame generators with wavelet masks $Q_m, m = 1, \ldots, 4+N$ such that $\mathcal{P}, \mathcal{Q}_m, m = 1, \ldots, 4+N$, satisfy (3.4). Although there is no Riesz-Féjer theorem in the multivariate setting, we are able to find additional Laurent polynomials $\tilde{P}_i$ to satisfy (3.7) for bivariate box spline functions (cf. [29]).

We next recall the definition of bivariate box spline functions on a direction set D. For instance, by letting $e_1 = (1,0), e_2 = (0,1), e_3 = e_1 + e_2, e_4 = e_1 - e_2, e_5 = (2,1), e_6 = (2,-1), e_7 = (1,2), e_8 = (1,-2)$, one can define D as the set of these vectors with some repetitions. Then the box spline ϕ_D associated with direction set D may be defined in terms of Fourier transform by

$$\hat{\phi}_D(\omega) = P_D(\frac{\omega}{2})\hat{\phi}_D(\frac{\omega}{2}), \tag{3.8}$$

where P_D is

$$P_D(\omega) = \prod_{\xi\in D} \frac{1 + e^{-i\xi\cdot\omega}}{2}.$$

We refer the interested readers to [7], [14] and [28] for many properties of box splines. An explicit polynomial representation of bivariate box splines enables us to evaluate these box splines easily [24, 28]. Note that it is easy to show that the mask P_D satisfies (3.6). To construct the associated tight framelets, we mainly find additional Laurent polynomials to satisfy (3.7). However, it is not an easy task as there is no existence theory nor a constructive procedure except for box splines on a three and a four direction mesh. This will be further explained in the next subsection.

3.2. The eight direction box spline. When using a box spline wavelet frame, we have the flexibility to choose a direction set. We can choose a box spline function with as many directions as possible to increase the redundancy. However, the more directions there are, the smoother the box spline function will be, the longer the length of the low pass and high pass filters are, and hence, more difficult it is to find tiny details in the image. Empirical results show that the wavelet frame based on box spline with eight directions is the ideal one for edge/feature/detail detection. In this paper we shall present a tight framelet based on box spline $\phi_8 := \phi_{D_8}$ with

$$D_8 = \{e_1, e_2, e_1 + e_2, e_1 - e_2, 2e_1 + e_2, 2e_1 - e_2, e_1 + 2e_2, e_1 - 2e_2\}. \tag{3.9}$$

Since D_8 contains eight directions, we call ϕ_8 an eight direction box spline. This box spline is new and has not been studied in the literature. It is a bivariate spline function of total degree ≤ 6, which is in C^5. Also ϕ_8 is compactly supported and nonnegative. All the integer translations of ϕ_8 are linearly dependent. Thus they are redundant. But they form a partition of unity after a scale. The mask $P_8 := P_{D_8}$ can be found easily and is

$$\begin{aligned} P_8(\xi,\eta) = &\left(\frac{1+e^{i\xi}}{2}\right)\left(\frac{1+e^{i\eta}}{2}\right)\left(\frac{1+e^{i(\xi+\eta)}}{2}\right)\left(\frac{1+e^{i(\xi-\eta)}}{2}\right) \\ &\left(\frac{1+e^{i(\xi+2\eta)}}{2}\right)\left(\frac{1+e^{i(2\xi+\eta)}}{2}\right)\left(\frac{1+e^{i(\xi-2\eta)}}{2}\right)\left(\frac{1+e^{i(2\xi-\eta)}}{2}\right). \end{aligned} \tag{3.10}$$

For convenience, we shall write $P_8(\xi,\eta) = \sum_{j,k} p_{j,k} e^{-ij\xi} e^{-ik\eta}$. To use Theorem 3.2, we need to show that (3.7) is satisfied for some $\widetilde{P}_i$. For box splines on a three and a four direction mesh, it is known that the polynomial equation (3.7) has a solution (cf. [29] and [26]). Furthermore, in [17], the researchers showed that (3.7) has a solution in general if the inequality in (3.6) is a strict. The researchers in [6] proposed using semi-definite programming (SDP) to find $\widetilde{P}_1, \cdots, \widetilde{P}_N$ satisfying (3.7). However, SDP is currently only able to solve this problem for small scales.

Recently, the researchers in [5] presented an algebraic approach proving that (3.7) has a solution for box splines on a three and a four direction mesh. For the box spline ϕ_8, it was challenging to solve equation (3.7) for a number of reasons. First, the number, N, of extra Laurent polynomials $\tilde{P}_j$ is unknown. The degrees of these polynomials are also unknown although our intuition is that the degrees should be less than or equal to 6, the degree of the 8 direction box spline ϕ_8. We solved (3.7) using brute force. We started with $N = 1$ and used Maple to try to solve the equation (3.7) but it was not successful. We then increased the value of N to 2 and did the same thing. The smallest value for which Maple could find a solution is $N = 10$, which corresponds to a large system of multivariate quadratic equations involving more than 50 variables. We then decoupled these equations and broke the system into smaller subsystems. Eventually, we were able to solve the system within a very small tolerance (e.g. 10^{-10}) and find ten Laurent polynomials $\widetilde{P}_j, j = 1, \cdots, 10$ to satisfy (3.7), i.e.

$$1 - \sum_{\nu \in \{0,\pi\}^2} |P_8(\omega+\nu)|^2 \approx \sum_{j=1}^{10} |\widetilde{P}_j(2\omega, 2\eta)|^2, \qquad \omega = (\xi,\eta) \in [0, 2\pi]^2.$$

The ten Laurent polynomials are given below:

$$\begin{aligned}
\widetilde{P}_1(\xi,\eta) &= \frac{42}{14561} - \frac{542}{4269} e^{i(\xi+4\eta)} + \frac{42}{14561} e^{2i\xi} + \frac{191}{1576} e^{i\xi},\\
\widetilde{P}_2(\xi,\eta) &= \frac{281}{1476} - \frac{51}{26513} e^{i(4\xi+\eta)} + \frac{281}{1476} e^{2i\eta} - \frac{605}{1597} e^{i(\xi+\eta)},\\
\widetilde{P}_3(\xi,\eta) &= \frac{1}{192} - \frac{9}{32} e^{i(2\xi+3\eta)} + \frac{1}{192} e^{4i\xi} + \frac{283}{1152} e^{2i(\xi+\eta)} + \frac{29}{1152} e^{2i\xi},\\
\widetilde{P}_4(\xi,\eta) &= \frac{192}{15731} - \frac{233}{19415} e^{i(3\xi+2\eta)} + \frac{192}{1573} e^{4i\eta} - \frac{172}{741} e^{2i\eta},\\
\widetilde{P}_5(\xi,\eta) &= \frac{139}{2849} - \frac{278}{2849} e^{i(\xi+3\eta)} + \frac{139}{2849} e^{2i\xi},\\
\widetilde{P}_6(\xi,\eta) &= \frac{76}{4195} - \frac{843}{3208} e^{i(3\xi+\eta)} + \frac{76}{4195} e^{2i\eta} + \frac{227}{1002} e^{i(\xi+\eta)},\\
\widetilde{P}_7(\xi,\eta) &= \frac{412}{2807} - \frac{211}{1364} e^{i(\xi+2\eta)} + \frac{412}{2807} e^{2i\xi} - \frac{263}{3788} e^{2i(\xi+\eta)} - \frac{263}{3788} e^{2i\eta},\\
\widetilde{P}_8(\xi,\eta) &= \frac{152}{2475} - \frac{288}{779} e^{2i(\xi+\eta)} + \frac{152}{2475} e^{2i\eta} + \frac{494}{2001} e^{i(\xi+\eta)},\\
\widetilde{P}_9(\xi,\eta) &= \frac{19}{15834} - \frac{100}{983} e^{3i(\xi+\eta)} - \frac{19}{15834} e^{3i\xi} + \frac{100}{983} e^{3i\eta},\\
\widetilde{P}_{10}(\xi,\eta) &= \frac{230}{10131} - \frac{230}{10131} e^{3i\xi}.
\end{aligned}$$

By Theorem 3.2, we will have 14 tight wavelet frame generators using the constructive steps in [29]. These 14 tight frames ψ^ℓ in terms of Fourier transform can be expressed by

$$\widehat{\psi_8^\ell}(\xi,\eta) = Q^\ell(\xi/2, \eta/2)\ \widehat{\phi_8}(\xi/2, \eta/2),\ \ell = 1, \cdots, 14, \tag{3.11}$$

where $Q^\ell(\xi,\eta) = \sum_j \sum_k q_{jk}^{(\ell)} e^{-ij\xi} e^{-ik\eta}$. In the following subsection, we explain how to obtain one low pass and several high pass filters from these ψ_8^ℓ and ϕ_8, and use them for edge detection.

3.3. Image decomposition and reconstruction. Our edge detector based on box spline frames involves three steps. First, we use the box spline wavelet frame to decompose the input image into many levels of subimages which consist of a low pass part and several high pass parts of the image. Next we set the low pass part to be zero and threshold the high pass parts. Finally, we use the resulting high pass parts to get the edge map. The motivation is that edges of an image are represented in high frequencies, while the smoothing parts of an image are represented in terms of translations and dilations of the refinable box spline function. Thus, we set the coefficients of the low pass part in terms of translations and dilations of the box spline to be zero. Meanwhile, since noise is also represented in high frequencies, we apply a percentage thresholding technique (see Algorithm 1) to remove some noise.

Next, we explain how to do image decomposition and reconstruction. For convenience, we use the 14 tight wavelet frame functions, $\{\psi^1, \cdots, \psi^{14}\}$ constructed in the previous section based on the box spline function ϕ_8, to illustrate the decomposition and reconstruction. For an image f with finite energy ($f \in L^2(\mathbb{R}^2)$), let $a_{j,\mathbf{k}}$ be the value of the inner product of f with the $\phi_{j,\mathbf{k}}(\cdot) := 2^{2j}\phi_8(2^j \cdot -\mathbf{k})$, i.e., $a_{j,\mathbf{k}} = \langle f, \phi_{j,k}\rangle$, for $\mathbf{k} \in \mathbb{Z}^2$ and $j \in \mathbb{Z}$. Note that since ϕ_8 is compactly supported and $\int \phi(x)dx = 1$, $a_{j,\mathbf{k}}$ can approximate the grayscale value at $\mathbf{k}$ when j is large enough. Similarly, let $b^\ell_{j,\mathbf{k}}$ be the value of the inner product of f with box spline wavelet framelets $\psi^\ell_{j,\mathbf{k}}(\cdot) := \psi^\ell(2^j \cdot -\mathbf{k})$'s for all $j \in \mathbb{Z}, \mathbf{k} \in \mathbb{Z}^2$ and $\ell = 1, \cdots, 14$, i.e., $b^\ell_{j,\mathbf{k}} = \langle f, \psi^\ell_{j,\mathbf{k}}\rangle$.

Recall we have

$$\phi_{j,\mathbf{m}}(\cdot) = \sum_{\mathbf{k}\in\mathbb{Z}^2} p_{\mathbf{k}-2\mathbf{m}}\phi_{j+1,\mathbf{k}}(\cdot) \quad \text{and} \quad \psi^\ell_{j,\mathbf{m}}(\cdot) = \sum_{\mathbf{k}\in\mathbb{Z}^2} q^\ell_{\mathbf{k}-2\mathbf{m}}\phi_{j+1,\mathbf{k}}(\cdot)$$

by using the refinable property (3.10) and wavelet frame construction (3.11) for all integers. Note that the refinable function ϕ and tight wavelet frames $\psi^1, \cdots, \psi^{14}$ are locally supported, and the coefficients $\{p_{\mathbf{k}-2\mathbf{m}}\}$ and $\{q^\ell_{\mathbf{k}-2\mathbf{m}}\}$ are finite sequences for all $\ell = 1, \cdots, 14$. Here $p_{\mathbf{k}-2\mathbf{m}}$'s and $q^\ell_{\mathbf{k}-2\mathbf{m}}$'s are associated with the coefficients of the low pass filter P and the high pass filters Q_ℓ respectively. Due to the limited space in this article, we refer to the webpage www.math.uga.edu/~mjlai/boxspline8.html for specific expressions of the low and high pass filters. By taking inner products on both sides of the above two equations with image function f, we obtain the following tight wavelet frame decomposition algorithm :

$$a_{j,\mathbf{m}} = \sum_{\mathbf{k}\in\mathbb{Z}^2} p_{\mathbf{k}-2\mathbf{m}}a_{j+1,\mathbf{k}} \quad \text{and} \quad b^\ell_{j,\mathbf{m}} = \sum_{\mathbf{k}\in\mathbb{Z}^2} q^\ell_{\mathbf{k}-2\mathbf{m}}a_{j+1,\mathbf{k}} \tag{3.12}$$

for all $j \in \mathbb{Z}, \mathbf{m} \in \mathbb{Z}^2$ and $\ell = 1, \cdots, 14$. Let X_j be the matrix associated with the $(j)^{th}$ level image containing $a_{j,k}, \forall k \in \mathbb{Z}^2_+$ with $|k| \le M$ (e.g., M = 512 for a 512 by 512 image) for all $j \in \mathbb{Z}$. Suppose that j is an integer large enough such that the given image f is approximately X_{j+1}, i.e. the pixel value $f_k \approx a_{j+1,k}$. Then the image decomposition procedure is to compute 2D convolution of P and each $Q_\ell, \ell = 1, \cdots, 14$ with the matrix X_{j+1}, i.e., we find

$$P * X_{j+1}, \quad Q_\ell * X_{j+1}, \ell = 1, \cdots, 14,$$

where $*$ stands for 2D convolution. We then downsample them by deleting all the odd number of rows and columns to obtain matrices X_j and $Y_{j,\ell}$ for $\ell = 1, \cdots, 14$.

Next, let us describe the reconstruction procedure. Due to the exact reconstruction, we have

$$\phi_{j+1,\mathbf{m}}(\cdot) = \sum_{\mathbf{k}\in\mathbb{Z}^2} \{p_{\mathbf{m}-2\mathbf{k}}\phi_{j,\mathbf{k}}(\cdot) + \sum_{\ell=1}^{8} q^\ell_{\mathbf{m}-2\mathbf{k}}\psi^\ell_{j,\mathbf{k}}(\cdot)\} \tag{3.13}$$

by using the perfect condition (3.4). By taking inner products on both sides of the above equation, we have the tight wavelet frame reconstruction algorithm:

$$a_{j+1,\mathbf{m}} = \sum_{\mathbf{k}\in\mathbb{Z}^2} \{p_{\mathbf{m}-2\mathbf{k}}a_{j,\mathbf{k}} + \sum_{\ell=1}^{N} q^\ell_{\mathbf{m}-2\mathbf{k}}a^\ell_{j,\mathbf{k}}\}. \tag{3.14}$$

Computationally, this can be done by upsampling the image $X_j, Y_{j,\ell}$ by 2, i.e., adding zero columns in between columns of X_j and $Y_{j,\ell}, \ell = 1, \cdots, 14$ and then add zero rows in between rows of the resulting matrices and then convolve with P and $Q_\ell, \ell = 1, \cdots, 14$.

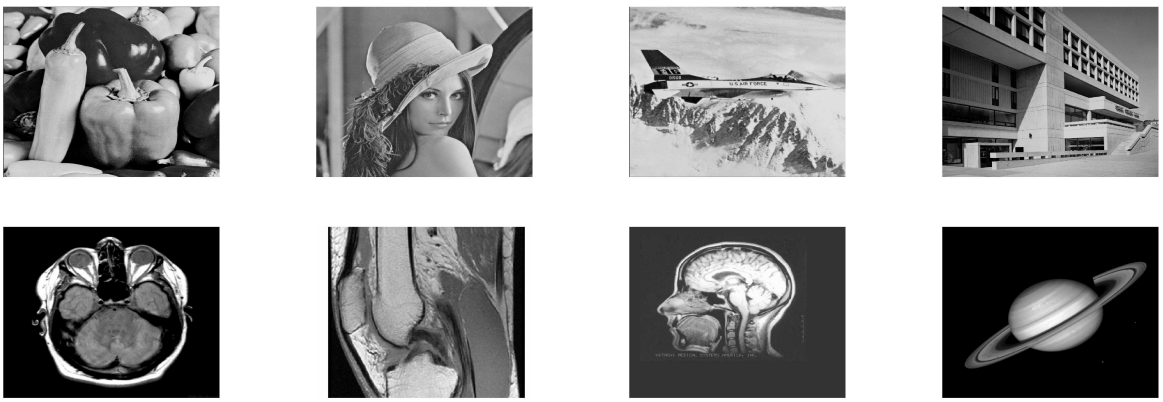

FIG. 3.1. *Eight testing images.*

Usually, X_j, $Y_{j,i}, i = 1, \cdots, \ell$ are called the low pass, and high pass parts of the image X_{j+1} respectively as they contain the low frequency and high frequency information of X_{j+1} respectively. If necessary, we can repeat the decomposition process several times by convolving the low pass image X_j with the low pass filter P and the high pass filters Q_ℓ's to get X_{j-1} and $Y_{j-1,\ell}, \ell = 1, \cdots, 14$ respectively. For simplicity, we do one level decomposition and reconstruction to demonstrate our algorithm.

3.4. Noise removal before edge detection. Images are usually contaminated by noise. It is sometimes necessary to remove noise from images before computing the edges. A classic method for image denoising is the wavelet shrinkage method which consists of using a hard or soft thresholding algorithm to trim the wavelet coefficients. In the following, we propose another approach based on the so-called weak orthogonal greedy algorithm (cf. [44]) to further reduce noise.

The main idea is to look for a sparse representation of a noisy image in a redundant wavelet frame system. Let $\Phi = [\phi_1, \cdots, \phi_n](n = 15)$ be a wavelet frame matrix consisting of the values of the framelet functions over discrete grids, i.e. $\phi_1, \cdots, \phi_n$ consist of the values of the refinable functions $\phi(\cdot + (j,k)), \psi^\ell(j,k), \ell = 1, \cdots, 14, (j,k) \in [1,M] \times [1,M]$ for an integer M. Let f be the image, $G_k(f)$ be the k^{th} approximation of f, and $R_k(f)$ be the residual of the k^{th} iteration.

ALGORITHM 1 (Percentage Thresholding Algorithm). *We begin with* $\Lambda_0 = \emptyset, R_0(f) = f, G_0(f) = 0$. *Choose a thresholding sequence* $\{t_1, t_2, \cdots\}$ *with all* $t_k \in (0,1]$.

- *Step 1. For* $k \geq 1$, *find* $M_k = \max_{i \notin \Lambda_{k-1}} |\langle R_{k-1}(f), \phi_i \rangle|$;
- *Step 2. Let* $\Lambda_k = \Lambda_{k-1} \cup \{i, |\langle R_{k-1}(f), \phi_i \rangle| \geq t_k M_k\}$;
- *Step 3. Let* $L_{\Lambda_k}(f)$ *the the best approximation (least squares approximation) of* $R_{k-1}(f)$ *in subspace* $S_{\Lambda_k} = span\{\phi_i, i \in \Lambda_k\}$.
- *Step 4. Update* $G_k = G_{k-1}(f) + L_{\Lambda_k}(f)$ *and* $R_k(f) = R_{k-1}(f) - L_{\Lambda_k}(f)$.
- *Step 5. If* $\|L_{\Lambda_k}(f)\|$ *is small enough, stop the algorithm. Otherwise we advance* k *to* $k+1$ *and go to Step 1.*

This algorithm differs from the weak orthogonal greedy algorithm in that in chooses more than one component per iteration. In this paper, we report some numerical results using the wavelet frame based on tensor product of symmetric quartic B-splines constructed in [8].

In our experiments, we first use the classic hard thresholding method to remove some noise based on wavelet frame decomposition and reconstruction. More specifically, we decompose an image into one low pass part as well as several high pass parts, and apply the hard thresholding technique to reduce noise from the high pass parts. A smoother image is reconstructed from the low pass part and the resulting high pass parts. Next we use the smoother image as f and the associated tight wavelet frame to form a wavelet frame matrix Φ and then apply Algorithm 1 for further noise reduction. In this experiment, we use a thresholding sequence $\mathbf{t} = \{t_0, t_1, t_2, t_3, \cdots\}$ with $t_i = rt_{i-1}$ with e.g. $r = 0.78$ and $t_0 = 0.9$ for $i = 1, 2, \cdots, 5$. Although the weak orthogonal greedy algorithm requires $\sum_{i \geq 1} t_i/i = \infty$ to converge, we only do 5 iterations to reduce noise. Since $\phi_i, i = 1, \cdots, n$ are just various wavelet framelets and their integer translations, the inner

products $\langle R_k, \phi_i \rangle$ are just convolution of ϕ_i with the image or the $(k-1)^{th}$ residual. In each iteration of Algorithm 1, we use t_k to form a thresholding $\epsilon_\ell = t_k M_\ell$ with M_ℓ being the largest inner product in absolute value in the ℓ^{th} high pass part of the image for $\ell = 1, \cdots, 14$.

The performance of the above Algorithm 1 is demonstrated using the eight images shown in Figure 3.1. All images have intensity range $[0, 255]$. We add white Gaussian noise with $\sigma = 20$ to all the images to simulate noisy images. We first apply the hard-thresholding method based on the wavelet frame mentioned above to reduce noise and find the best denoised image in terms of the standard Peak-Signal-to-Noise Ratio (PSNR). Then we use Algorithm 1 to further reduce noise. In the following table, we report the PSNR before and after using Algorithm 1.

Table 1. PSNR before and after applying Algorithm 1

	Peppers	Lena512	F16	Bank
Before	30.25	30.66	30.38	29.47
After	30.37	31.14	30.53	29.53
NZC	15.21%	5.43%	21.67%	27.88%
	Brain	Knee	MRI	Saturn
Before	32.08	30.12	32.48	35.28
After	32.50	30.23	32.80	35.65
NZC	7.62%	23.73%	4.99%	0.523%

Certainly, when using a multi-level decomposition and reconstruction of wavelet frames, one may get slightly better PSNR values than those in Table 1. We leave them to interested readers. An advantage of using this approach for image denoising is that one only needs about 25% or less nonzero coefficients of a tight wavelet frame to represent a denoised image. In Table 1, we list the percentage of nonzero coefficients (NZC) in a wavelet frame representation for each image. Here the NZC is the ratio of the number of nonzero coefficients over the size of images after denoising.

3.5. Image edge detection. We reconstruct the edges of an image based on the zero low pass part and the high pass parts after a percentage thresholding technique which only keeps the lowest 50% largest coefficients. Here is the outline of image edge detection procedure:

ALGORITHM 2 (Box Spline Edge Detector). *We apply the following steps for an input image f:*

1. *Reduce noise to get a cleaner image $\tilde{f}$ by using Algorithm 1.*
2. *Apply the tight wavelet frame to decompose the image $\tilde{f}$ into one low pass and various high pass sub-images.*
3. *Set the low pass part to be zero and keep the lowest 50% of the coefficients in absolute value of each of the high pass parts.*
4. *Reconstruct image $\hat{f}$ from the zero low pass and the thresholded high pass components.*
5. *Use k-means classification with two classes to automatically classify $\hat{f}$ into two categories: either* 0 *or* 1*.*
6. *Clean up by removing all short isolated edges.*

Comments.

- The only parameter in the proposed Algorithm 2 is the percentage of high pass component coefficients to keep. We understand that fine tuning of this threshold might lead to better results, but to make it simple, we just use 50%. It turns out that the numerical results are consistently satisfactory already. Moreover, the last step in Algorithm 2 is also applied to other edge detectors.
- Note that noise exists in both high frequency and low frequency parts. Although cutting off a portion of the high frequency part as we do in the third step of the above edge detection algorithm does remove some high frequency noise, there is still some left. To avoid false edges and other artifacts due to noise, we apply Algorithm 1 to reduce noise before detecting edges. This denoising procedure however makes the overall edge detection approach scale variant.
- The k-means classification in the fifth step of the algorithm is to automatically obtain a binary edge map from the result of the fourth step of Algorithm 2. It does not help with detecting edges or fine features more accurately.

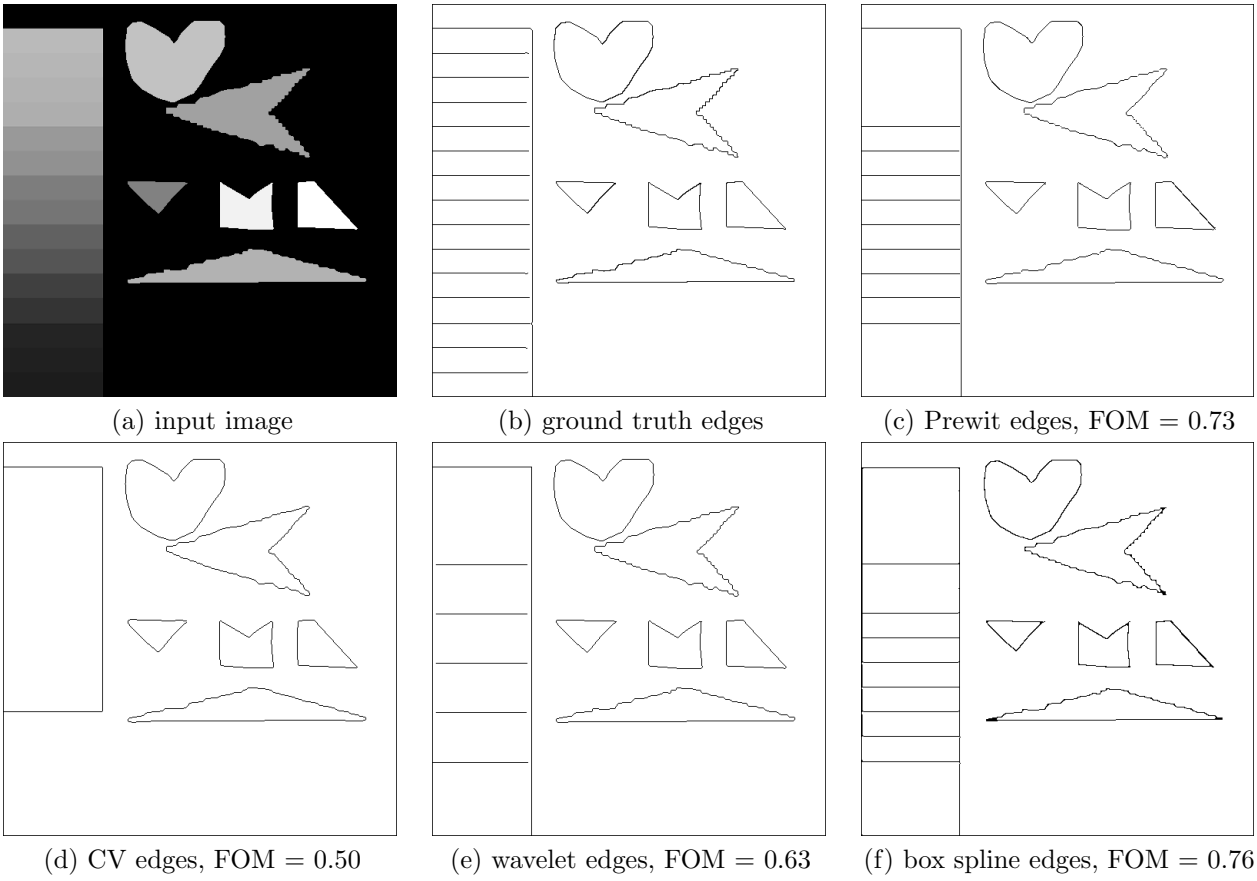

(a) input image (b) ground truth edges (c) Prewit edges, FOM = 0.73

(d) CV edges, FOM = 0.50 (e) wavelet edges, FOM = 0.63 (f) box spline edges, FOM = 0.76

FIG. 4.1. *Comparison of four edge detectors on a synthetic image.*

4. Numerical experiments. This section consists of three sets of experimental results. In subsection 4.1, we compare the proposed box spline edge detector with some selected edge detectors: Prewit, Canny, Chan-Vese, wavelet [32] and shearlet [47]. In subsection 4.2, we test the performance of the proposed method on detecting edges of noisy images. Subsection 4.3 and 4.4 focus on detecting Dirac and hidden edges respectively. The last subsection discusses the application of the box spline based edge detector on object identification.

4.1. Comparison of several edge detection methods. We demonstrate the advantage of the proposed box spline edge detection method through comparing with some methods mentioned in section 2. While there has been some attempts on proposing quantitative measures for the performance of an edge detector, there seems to be no consensus on which one is the best. We select two popular ones: Pratt's figure of merit (FOM) [38] and probability of detection (P_D) [1], the probability for an edge detector to find true edges. Computation of both of these measures require ground truth edges. Thus, we create one image with ground truth edges outlined by hand (Figure 4.1).

Pratt's figure of merit is a measure describing the distance from the detected edges to the ground truth edges. It is defined as

$$FOM = \frac{1}{\max(n_d, n_g)} \sum_{k=1}^{n_g} \frac{1}{1 + \alpha d(k)}$$

where n_d, n_g are the number of points on the detected and ground truth edges respectively, $d(k)$ is the distance from the kth detected edge point to the actual ground truth edges. α is a scaling constant that we set as $1/9$. The larger FOM the better.

Edge detection can also be cast as a hypothesis testing problem that determines if an image pixel is

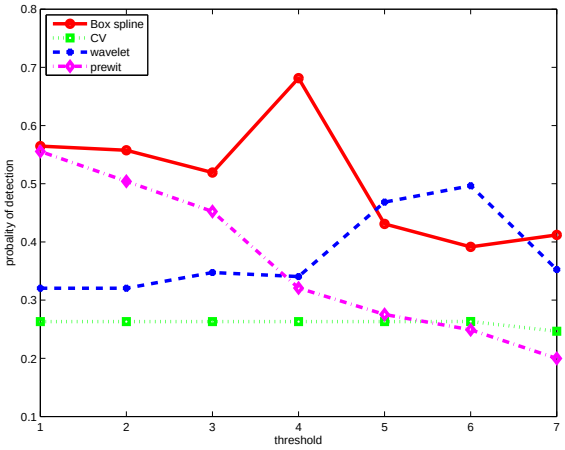

FIG. 4.2. *Compare probability of detection of the four edge detectors on various parameters. The test image is the one shown in Figure 4.1(a).*

(a) input image (b) shearlet edges (c) Canny edges

(d) Chan-Vese edges (e) wavelet edges (f) box spline edges

FIG. 4.3. *Comparison of five edge detectors on Lena image.*

on edge or not. The efficiency of edge detection can thus be evaluated using a metric from statistics: the probability of correct edge detection P_D. It measures the ability of an edge detection method in correctly locating actual edges. Let M_d, M_g be the detected and the ground truth binary edge maps with 1,0 intensity representing edge, and non-edge respectively. Then P_D is defined as

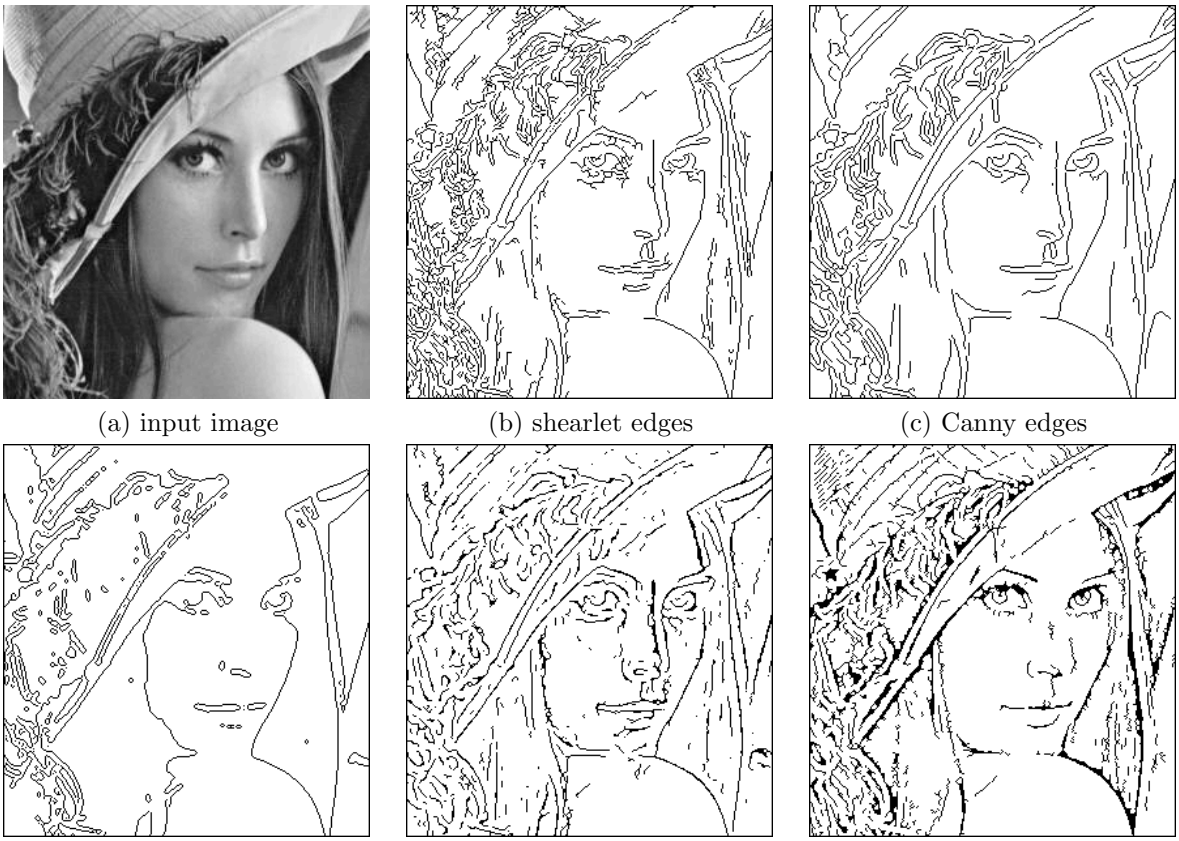

(a) input image (b) shearlet edges (c) Canny edges

(d) Chan-Vese edges (e) wavelet edges (f) box spline edges

FIG. 4.4. *Zoom in comparison of five edge detectors on the Lena image shown in Figure 4.3.*

$$P_D = Prob(M_d = 1 | M_g = 1) = \frac{Prob(M_d = 1, M_g = 1)}{Prob(M_g = 1)}.$$

To avoid the intervention of the denoising process to the performance evaluation of edge detection methods, we start with a simulated clean image (shown in Figure 4.1 (a)) with ground truth edges (Figure 4.1 (b)). It contains objects of various shapes and rectangular boxes with gradually changing intensities. We apply Prewit, Chan-Vese, wavelet and box spline edge detection methods to (a) under each method's best parameter setting and obtain results as shown in (c)-(f). It can be seen that the box spline result has the highest FOM and is also visually the closest to the ground truth edges.

Results in Figure 4.1 are computed using each method's best possible parameter selection. Note that more horizontal lines on the left can be detected by lowering the threshold value, but due to the fact that those areas have low intensities, and low contrast, one has to set the threshold to be extremely low to detect those horizontal lines. As a result, we pay the price of having broken and/or non-smooth edges almost everywhere at the geometries on the right hand side. We thus present the results that have the best overall appearance. In practice and in general, one most likely just chooses an ad hoc parameter. In Figure 4.2, we compare P_D of the four edge detection methods under seven different ad hoc parameters. One can see that the box spline edge detection method has significantly higher P_D than the other four methods except for two out of seven of the wavelet edge detection results.

Next, we compare those edge detectors on natural images with more details (Figure 4.3 to Figure 4.8). No ground truth edges are available for quantitative comparison, but visual comparison shows that box spline method performs better in catching fine edges. See for instance the edges of Lena's hair and eyes in Figure 4.4 and those of table cloth, pants, and the face in Figure 4.6, as well as the edges of the textures and plants in Figure 4.8.

(a) input image (b) shearlet edges (c) Canny edges

(d) Chan-Vese edges (e) wavelet edges (f) box spline edges

FIG. 4.5. *Comparison of five edge detectors on Barbara image.*

From a computation time perspective, the proposed algorithm is indeed slower than Canny and Prewitt algorithms. Canny and Prewitt use two convolutions (x-direction and y-direction) while our algorithm uses 15 convolutions with one low pass and 14 high pass box spline filters. The sizes of our filters are also bigger. The current non-optimized implementation of the proposed algorithm is about 8 times as expensive as the Canny and Prewitt algorithms on average. It is about 8 times and 5 times as expensive as the wavelet and shearlet based method respectively. However, it is comparable with that of the Chan-Vese method.

Note that the wavelet [32] and shearlet [47] methods detect edges by analyzing the change of the transform coefficients across different scales. They are very different from the proposed edge detector based on low and high pass filters designed using box spline frames. One can also use the low and high pass filters in discrete wavelets such as Haar, D4, D6 and biorthogonal 9/7 in the proposed edge detector scheme to compute edges. We did the experiments but the performance is not comparable. We have also inserted discrete shearlet kernels from fast finite shearlet transform (FFST) toolbox [19] into the proposed edge detection, but the results are not as good as those in [47]. We thus do not include them here.

4.2. Edge detection for noisy images. We also test the performance of the proposed edge detection method on various noisy images. Next in Figure 4.9, we show the robustness of the proposed edge detector to noise by exhibiting edges detected from noisy images with SNR as low as 9. White Gaussian noise with standard deviation $\sigma = 40$ is added to each of the three clean image with intensity in $[0, 255]$. For each of the noisy images, we apply a standard wavelet frame denoising method (hard thresholding) to obtain a cleaner image which is fed into Algorithm 1 for further denoising if necessary. We then apply Algorithm 2 on the denoised image to detect edges.

One can see that most of the edges/features are still detected correctly. However, we do see some artifacts and lost edges due to the deterioration of the input images.

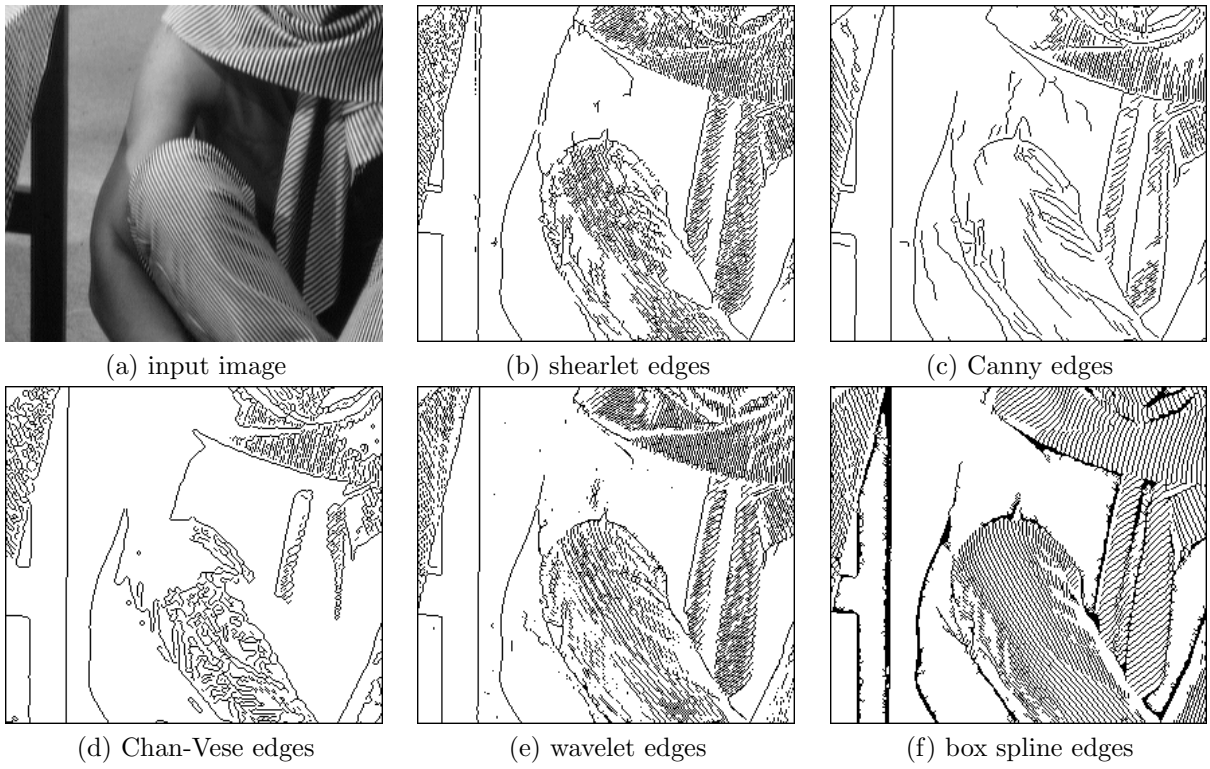

(a) input image (b) shearlet edges (c) Canny edges

(d) Chan-Vese edges (e) wavelet edges (f) box spline edges

FIG. 4.6. *Zoom in comparison of five edge detectors on the Barbara image shown in Figure 4.5.*

4.3. Dirac edges. It is well-known that the gradient based edge detectors such as Canny and Prewit fail to detect Dirac edges (locations with momentary intensity changes) accurately. They mistakenly treat locations to the left and the right side of Dirac edges as a discontinuity in intensity, and thus detect double step edges instead of Dirac edges. Our box spline wavelet frame detector can find such Dirac edges exactly. We show one example here. The left panel of Figure 4.10 is a testing image. Our box spline edge detector finds the exact edges appear exactly the same as the left panel of Figure 4.10.

4.4. Application to hidden edge detection. We now apply the box spline wavelet frame edge detector to find hidden edges, i.e., locations with some kind of discontinuous derivatives of image intensity. Detecting such edges has important applications, for instance aircraft surface manufacturing. To reduce the turbulence, the surface of the body of an aircraft needs to be C^2 smooth to avoid generating singularities of airflows. One way to find defects in the surface of an aircraft body is to find locations with discontinuous first or second order derivatives, i.e., hidden edges. In this subsection, we artificially create a surface with discontinuous first order derivatives. For example,

$$z_1(x,y) = \begin{cases} (x-1)^2 + (y-1)^2 - 0.5, & \text{if } (x-1)^2 + (y-1)^2 > 0.5, \\ 0, & \text{otherwise.} \end{cases}$$

over $(x,y) \in [0, 2.55]^2$. The 3D graph and the 2D intensity image of the function $z_1(x,y)$ are shown in the left and the right panel of Figure 4.11 respectively.

From the 2D intensity image, we hardly see any edges. However, from the 3D surface, we can easily see the places where the first order derivatives are discontinuous. As another example, let

$$z_2(x,y) = \begin{cases} (x+y-1.5)^2 - 0.5, & \text{if } (x+y-1.5)^2 > 0.5, \\ 0, & \text{otherwise,} \end{cases}$$

over $(x,y) \in [0, 2.55]^2$. The graph and the image of the function $z_2(x,y)$ are shown in Figure 4.12. Hidden edges are displayed in Figure 4.13.

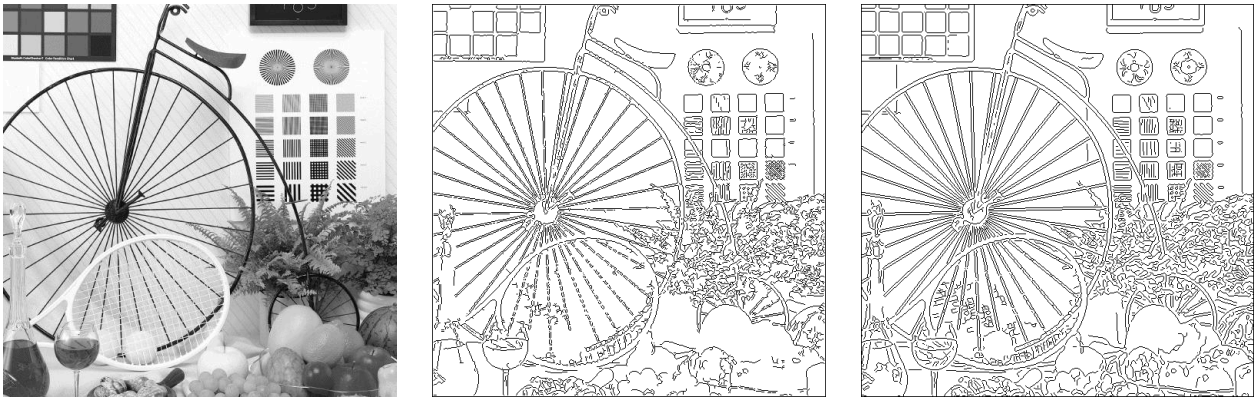

(a) input image (b) shearlet edges (c) Canny edges

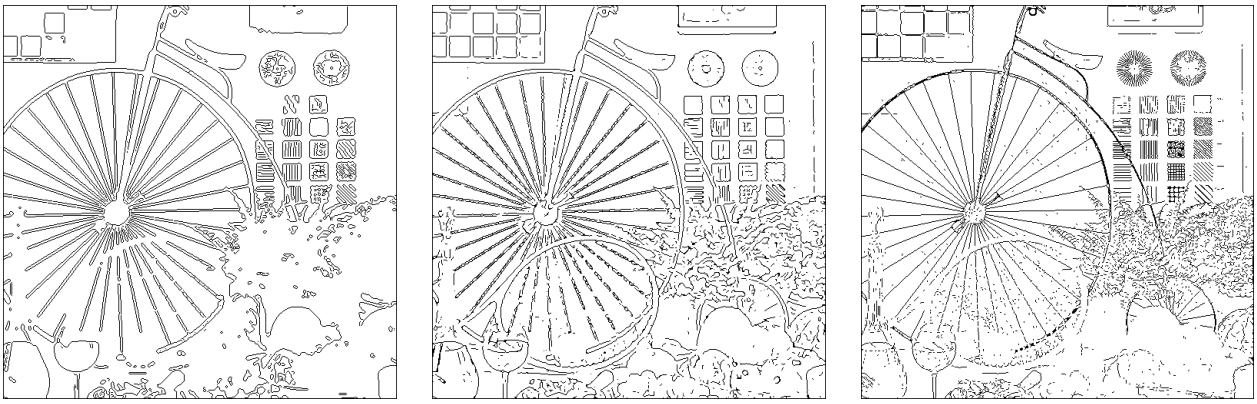

(d) Chan-Vese edges (e) wavelet edges (f) box spline edges

FIG. 4.7. *Comparison of five edge detectors on a bike image.*

We next present an example to detect hidden edges with discontinuous second order derivatives. The synthetic example is as follows.

$$z_3(x,y) = \begin{cases} ((x-1)^2+(y-1)^2-0.35)^2, & \text{if } (x-1)^2+(y-1)^2 \geq 0.35, \\ 0.125-((x-1.05)^2+(y-1)^2)^2, & \text{if } ((x-1.05)^2+(y-1)^2)^2 \leq 0.125, \\ 0, & \text{otherwise,} \end{cases}$$

over $(x,y) \in [0, 2.55]^2$. The graph and the image of the function $z_3(x,y)$ are shown in Figure 4.14 from which we can hardly see by naked eyes any irregularities or defects of the surface. However, our edge detector reveals hidden edges where possible defects may be located (Figure 4.15).

4.5. Application to object identification. The results of the box spline edge detector can be used for feature extraction, object identification, region segmentation, etc. In this subsection, we provide one example of practical application: to segment objects of interest from medical images.

As shown in Figure 4.16, starting with a 8-bit gray scale (valued in between 0 and 255) cardiac image (top left), we first use the proposed box spline edge detector to create a 1-bit (valued 0 or 1) edge mask (top right), followed by a cleaning up process to remove isolated edges (bottom left). To get the two objects of interest in the center of the image, we drop a small box inside each of the two objects, and grow the regions [46] until it touches the borders of the objects. The results are shown in the bottom right panel. Applying region growing segmentation to the 1-bit 0-1 edge mask is better than to the 8-bit gray scale image as borders of the objects of interest are more reliable and ready to be used in the 1-bit edge map. One may calculate the areas of the regions of interest for medical image analysis purpose afterwards.

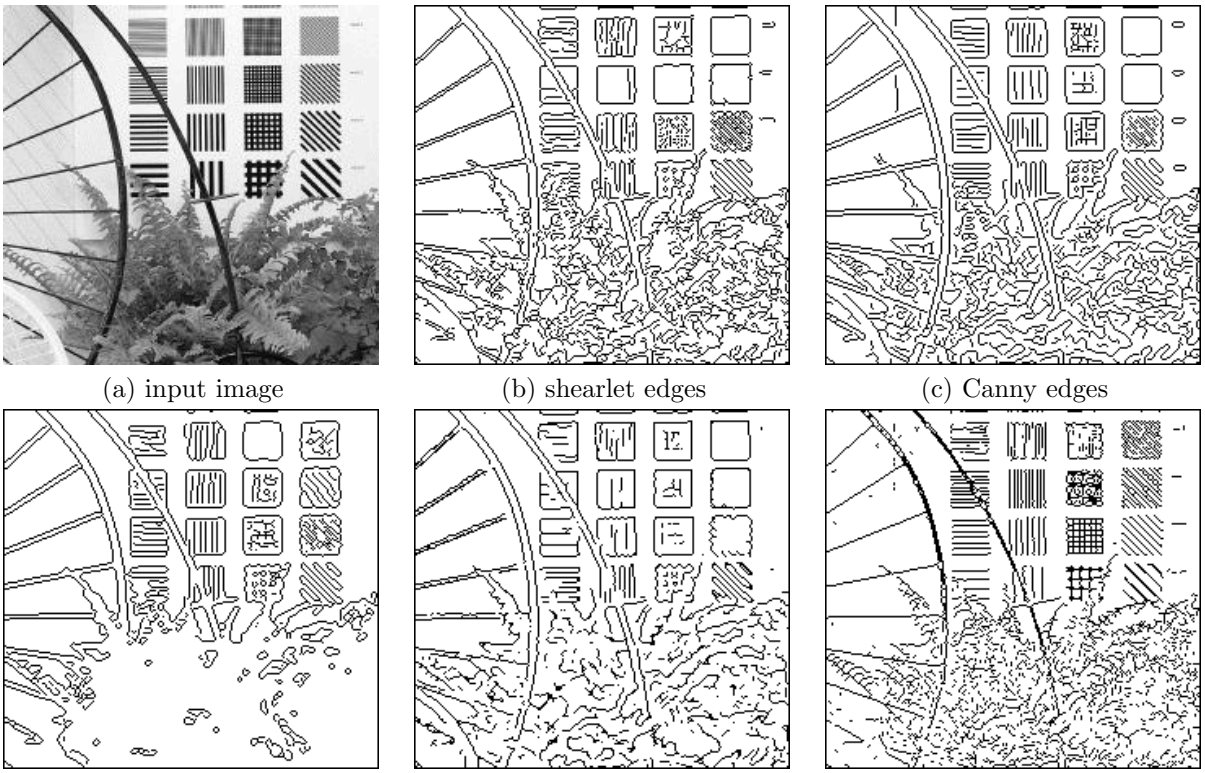

(a) input image (b) shearlet edges (c) Canny edges

(d) Chan-Vese edges (e) wavelet edges (f) box spline edges

FIG. 4.8. *Zoom in comparison of five edge detectors on the bike image shown in Figure 4.7.*

5. Conclusions. We present an edge detection algorithm based on a new eight direction box spline tight frame constructed using the theory in [29]. The construction of tight wavelet frames based on this eight direction box spline is nontrivial as there is no theory to guarantee the existence of a solution to the polynomial equation (3.7). Also, how to find a solution for a general polynomial equation (3.7) is still open. We use a brute force method to solve it. Once the framelets are found, computing edges based on these framelets is very simple and does not need complicated optimization criteria. It applies box spline based wavelet transforms to decompose a given image into one low pass and several high pass components. When there is no noise, edges are only the inverse wavelet transform of the high pass components. When noise exists, one needs some thresholds to separate true edges from noises, both of which belong to high pass components. Quantitative and qualitative comparison with several other existing edge detectors demonstrate the effectiveness and efficiency of the proposed method in detecting step edges. Our edge detector is also able to detect Dirac edges and hidden edges. In addition, we show that the proposed method is robust to noise. Finally, we apply the edge detector to object identification.

6. Acknowledgments. The first author is partially supported by NIH grant 1R21EB016535-01. The second author would like to thank Dr. Kyunglim Nam for her work in computing wavelet frame coefficients and implementing many box spline and B-spline wavelet frames. In addition, the second author also thanks Dr. Alexander Petukhov for the discussion on weak orthogonal greedy algorithms. In addition, we thank Drs. Sung Ha Kang, George Biros and Wei Zhu for providing us with the medical image studied in this paper. The authors appreciate the anonymous referees for the valuable comments that help improve the presentation of the paper.

REFERENCES

[1] K. E. Abdou and K.K. Pratt. Quantitative design and evaluation of enhancement/thresholding edge detectors. *Proc. of IEEE*, 67(5):753–763, 1979.

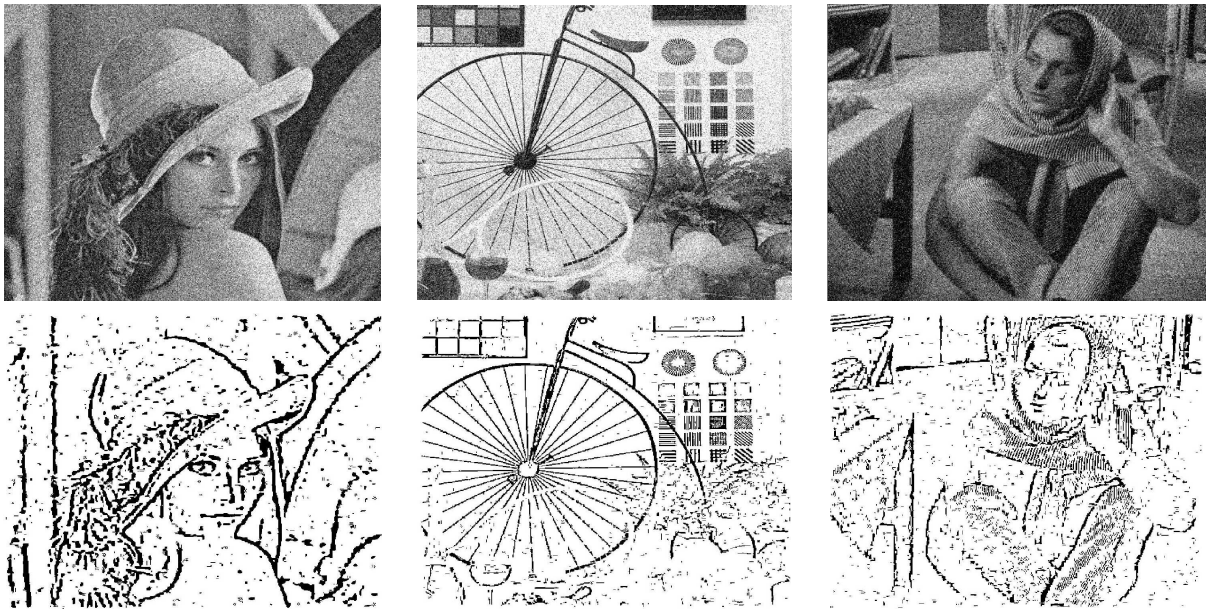

FIG. 4.9. *Edges (second row) detected from noisy images (first row).*

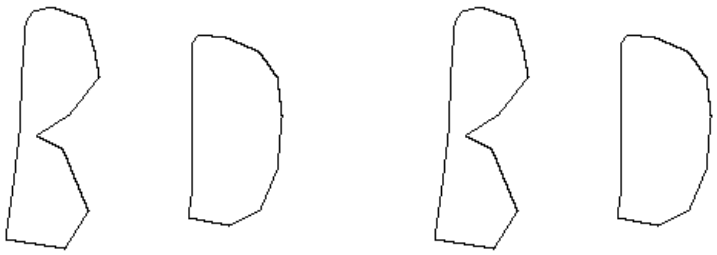

FIG. 4.10. *The proposed box spline edge detector is able to detect Dirac edges.*

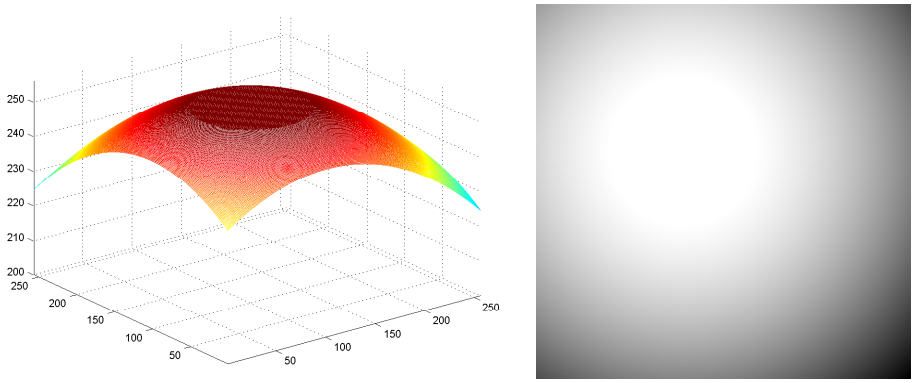

FIG. 4.11. *The graph (left) and the image (right) of function z_1 with discontinuous derivatives around a circle.*

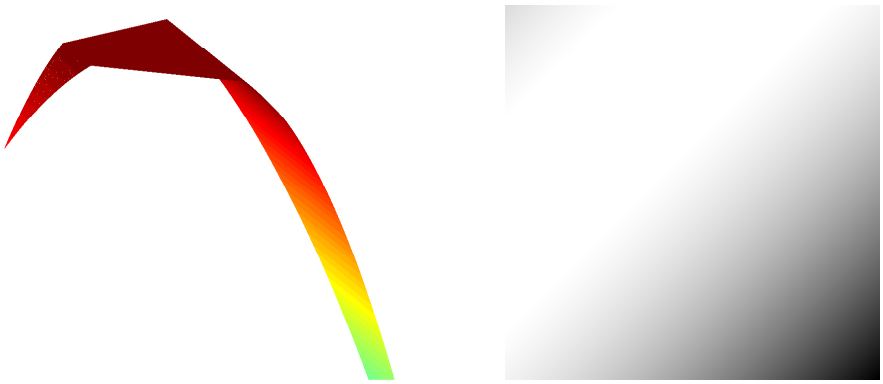

FIG. 4.12. *The graph (left) and the image (right) of function z_2 with discontinuous derivatives at two lines.*

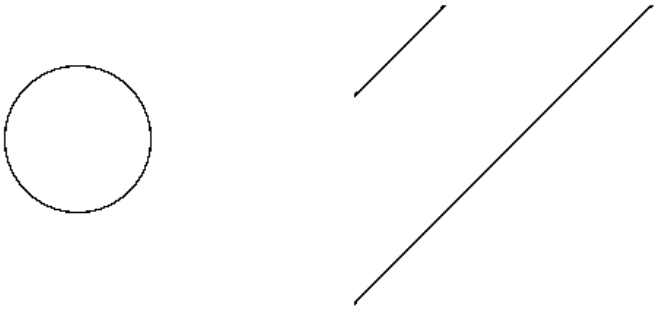

FIG. 4.13. *Locations of hidden edges of the images in Figures 4.11 (left) and 4.12(right).*

[2] L. Ambrosio and V. M. Tortorelli. On the approximation of free discontinuity problems. boll. *Un. Mat. Ital. B*, 7(6):105–123, 1992.

[3] J. Canny. A computational approach to edge detection. *IEEE Trans. Pattern Analysis and Machine Intelligence*, 8:679–714, 1986.

[4] T. F. Chan and L. A. Vese. Active contours without edges. *IEEE Trans. Image Processing*, 10(2):266–277, 2001.

[5] M. Chrina, M. Putinar, C. Scheiderer, and J. Stöckler. An algebraic perspective on multivariate tight wavelet frames. *Constructive Approximation*, to appear, 2013.

[6] M. Chrina and J. Stöckler. Construction of tight wavelet frames by semidefinite programming. *J. Approx. Theory*, 162:1429–1449, 2010.

[7] C. K. Chui. *Multivariate splines*, volume 54 of *CBMS-NSF Regional Conference Series in Applied Mathematics*. Society for Industrial and Applied Mathematics (SIAM), Philadelphia, PA, 1988. With an appendix by Harvey Diamond.

[8] C. K. Chui and W. He. Compactly supported tight frames associated with refinable functions. *Appl. Comput. Harmon. Anal.*, 8(3):293–319, 2000.

[9] C. K. Chui and W. He. Construction of multivariate tight frames via Kronecker products. *Appl. Comput. Harmon. Anal.*, 11(2):305–312, 2001.

[10] C. K. Chui, W. He, and J. Stöckler. Compactly supported tight and sibling frames with maximum vanishing moments. *Appl. Comput. Harmon. Anal.*, 13(3):224–262, 2002.

[11] C. K. Chui, W. He, and J. Stöckler. Compactly supported tight and sibling frames with maximum vanishing moments,. *Appl. Comput. Harmon. Anal.*, 13:224–262, 2002.

[12] I. Daubechies. *Ten lectures on wavelets*, volume 61 of *CBMS-NSF Regional Conference Series in Applied Mathematics*. Society for Industrial and Applied Mathematics (SIAM), Philadelphia, PA, 1992.

[13] I. Daubechies, B. Han, A. Ron, and Z. Shen. Framelets: Mra-based constructions of wavelet frames. *Appl. Comput. Harmon. Anal.*, 14(1):1–46, 2003.

[14] C. de Boor, K. Hölig, and S. Riememschneider. *Box Splines*. Springer Verlag, 2003.

[15] R. Deriche. Fast algorithms for low-level vision. *IEEE Tran. Pattern Anal. Mach. Intell.*, 12(A):78–87, 1990.

[16] G. Easley, D. Labate, and W.Q. Lim. Sparse directional image representations using the discrete shearlet transform. *Appl. Comput. Harmon. Anal.*, 25:2546, 2008.

[17] J. Geronimo and M. J. Lai. Factorization of multivariate positive laurent polynomials. *, Journal of Approximation Theory*, 139:327–345, 2006.

[18] W. Guo and F. Huang. A local mutual information guided denoising technique and its application to self-calibrated

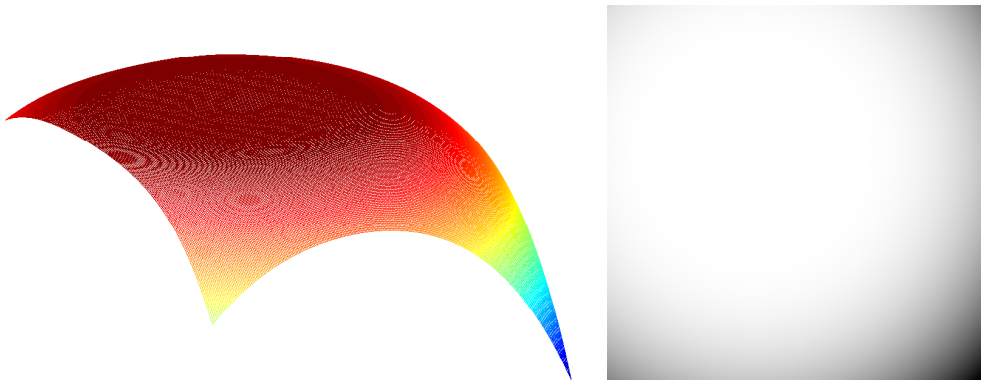

FIG. 4.14. *The graph (left) and the image (right) of function z_3 with discontinuous derivatives at two circles.*

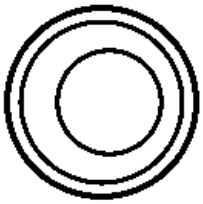

FIG. 4.15. *Hidden edges found from the image in Figure 4.14 using the proposed box spline edge detector.*

partially parallel imaging. *MICCAI, Part II, LNCS 5242*, pages 939–947, 2008.

[19] S. Häuser. Fast Finite Shearlet Transform, February 2012.

[20] W. He and M. J. Lai. Construction of bivariate compactly supported biorthogonal box spline wavelets with arbitrarily high regularities. *Applied and Computational Harmonic Analysis*, 6:53—74, 1999.

[21] B. Jahne, H. Scharr, and S. Korgel. Principles of filter design. *In B. Jahne, H. HauEecker, and P. GeiEJer, eds., Computer Vision and Applications, vol-volume 2, Signal Processing and Pattern Recognition, chapter 6, Academic Press, San Diego*, pages 125–151, 1999.

[22] J. J. Koenderink and A. J. van Doom. Generic neighborhood operators. *IEEE Trans. PAMI*, 14(F):597–605, 1992.

[23] D. Labate, W.-Q Lim, G. Kutyniok, and G. Weiss. Sparse multidimensional representation using shearlets. *Proc. SPIE Wavelets XI*, 5914:254262, 2005.

[24] M. J. Lai. Fortran subroutines for B-nets of box splines on three- and four-directional meshes. *Numer. Algorithms*, 2(1):33–38, 1992.

[25] M. J. Lai. Construction of multivariate compactly supported prewavelets in l_2 spaces and pre-riesz basis in sobolev spaces. *Journal of Approximation Theory*, 142:83—115, 2006.

[26] M. J. Lai and K. Nam. On the number of tight wavelet framelets associated with multivariate box splines. *Journal of Approximation Theory and its Application*, 2008.

[27] M. J. Lai and A. Petukhov. Method of virtual components in the multivariate setting. *Journal of Fourier Analysis and Its Applications*, 16:471–494, 2010.

[28] M. J. Lai and L. L. Schumaker. *Spline Functions over Triangulations*. Cambridge University Press, 2007.

[29] M.-J. Lai and J. Stöckler. Construction of multivariate compactly supported tight wavelet frames. *Appl. Comput. Harmon. Anal.*, 21(3):324–348, 2006.

[30] S. Lanser and W. Eckstein. Eine modification des deriche-verfahrens zur kantendetektion. *B. Radig, ed., Mustererkennung 1991, vol. 290 of Informatik Fachberichte, DAGM Symposium, Munchen, Springer, Berlin*, pages 151–158, 1991.

[31] S. Mahmoodi. Edge detection filter based on mumford-shah green function. *SIAM J. Imaging Sciences*, 5(1):343–365, 2012.

[32] S. Mallat and S. Zhong. Characterization of signals from multiscale edges. *IEEE. Trans. Patt. Anal. Machine Intell.*, 14:710–732, 1992.

[33] D. Marr and E. Hildreth. Theory of edge detection. *Proc. Royal Society, London*, pages 187–217, 1980.

[34] D. Mumford and J. Shah. Optimal approximation by piecewise smooth functions and associated variational problems.

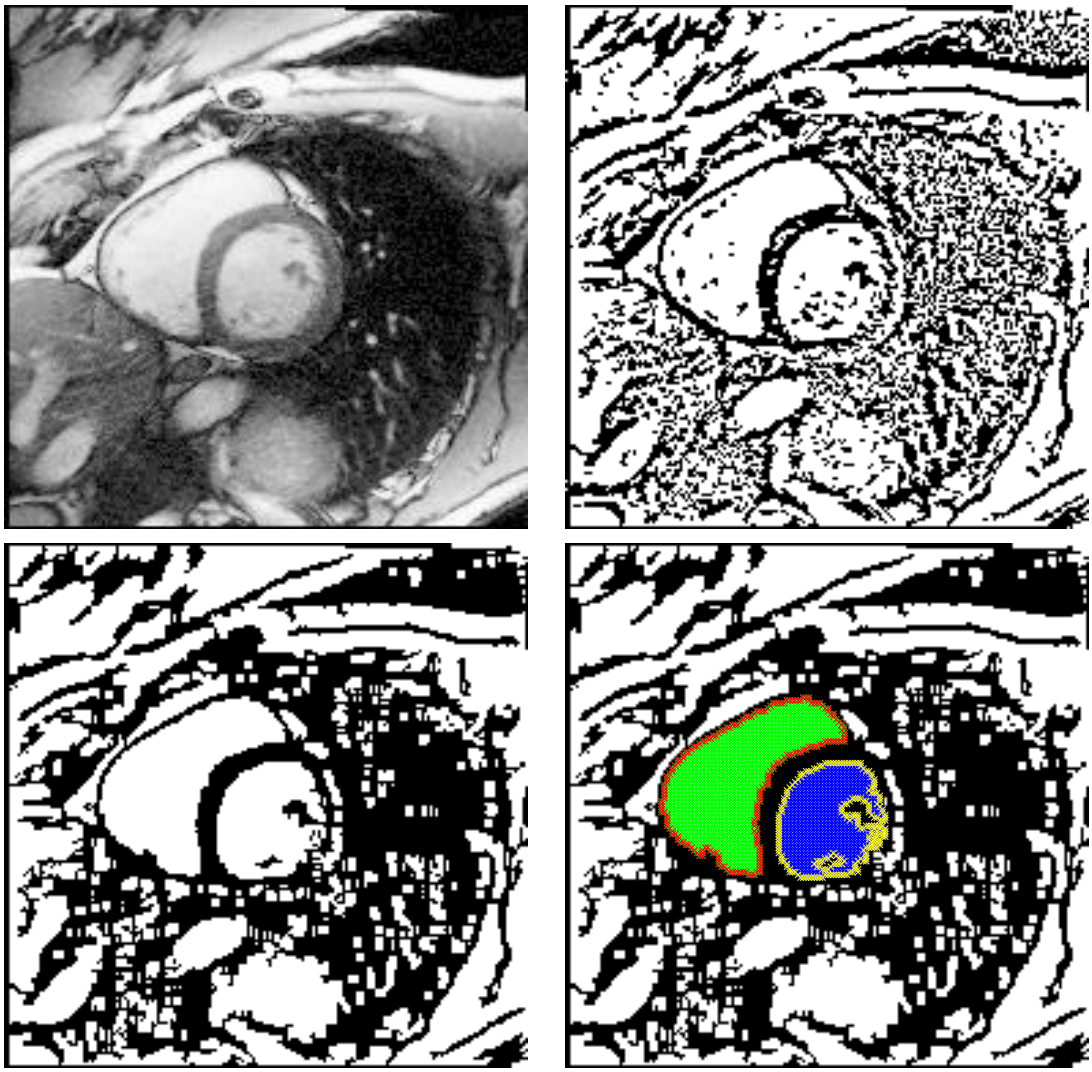

FIG. 4.16. *A medical image (top left), the resulting image based on box spline tight-wavelet frame detector (top right), cleaner edges (bottom left), and the outline of two regions of interest (bottom right).*

Comm. Pure Appl. Math., 42:557–685, 1989.

[35] K. Nam. *Tight Frame Construction and Its Application for Image Processing.* PhD thesis, University of Georgia, 2005.

[36] S. Osher and J. A. Sethian. Fronts propagating with curvature-dependent speed: Algorithms based on hamilton-jacobi formulations. *J. Comput. Phys.*, 79:12–49, 1988.

[37] I. Pitas and A.N. Venetsanopoulos. Nonlinear digital filters: Principles and applications. *Kluwer Academic Publishers*, 1990.

[38] W. K. Pratt. Digital image processing. *New York: Wiley-Interscience*, 1978.

[39] D. Qi, F. Guo, and L. Yu. Medical image edge detection based on omnidirectional multi-scale structure element of mathematical morphology. *IEEE International Conference on Automation and Logistics*, pages 2281–2286, 2007.

[40] A. Ron and Z. Shen. Compactly supported tight affine spline frames in $L_2(\mathbf{R}^d)$. *Math. Comp.*, 67(221):191–207, 1998.

[41] A. Ron and Z. Shen. Construction of compactly supported affine frames in $l_2(r^d)$,. In *Advances in Wavelets*, 1998.

[42] J. Serra. Image analysis and mathematical morphology. *Academic Press*, 1982.

[43] W. Stefan, R. A. Renaut, and A. Gelb. Improved total variation-type regularization using higher-order edge detectors. *SIAM Journal on Imaging Sciences*, 3(2):232–251, June 2010.

[44] V. N. Temlyakov. Greedy approximation. *Acta Numer*, 17:235409, 2008.

[45] B. Tian, H. Yuan, and X. Yue. Feature extraction algorithm for space targets based on fractal theory. *Second International on Space Information Technology, SPIE-INT SOC Optical Engineering*, 6795:79518–79518, 2007.

[46] S. Umbaugh. Computer vision and image processing: A practical approach using cviptools. 1997.

[47] S. Yi, D. Labate, R. G. Easley, and H. Krim. A shearlet approach to edge edge analysis and detection. *IEEE trans. Imag. Proc.*, 18(5):929–941, 2009.

[48] L. Zhai, S. Dong, and H. Ma. Recent methods and applications on image edge detection. *International Workshop on Geoscience and Remote Sensing*, pages 332 – 335, 2008.

[49] L. Zhang, A. Butler, and C. Sun. Fractal dimension assessment of brain white matter structural complexity post stroke in relation to upper-extremity motor function. *Brain Research*, 1228(4):229–240, 2008.

[50] D. Ziou and S. Tabbone. Edge detection techniques - an overview. *International Journal of Pattern Recognition and Image Analysis*, 8:537–559, 1998.